Rod-like colloids and polymers in shear flow: a multi-particle-collision dynamics study

Rod-like colloids and polymers in shear flow: a multi-particle-collision dynamics study

R G Winkler[1]**, K Mussawisade, M Ripoll and G Gompper**

Institut für Festkörperforschung, Forschungszentrum Jülich, D-52425 Jülich, Germany

E-mail: r.winkler@fz-juelich.de

Abstract
The effect of the hydrodynamic interaction on the dynamics of flexible and
rod-like polymers in solution is investigated. The solvent is simulated by the
multi-particle-collision dynamics (MPCD) algorithm, a mesoscale simulation
technique. The dynamics of the solvent is studied and the self-diffusion
coefficient is calculated as a function of the mean free path of a particle.
At small mean free paths, the hydrodynamic interaction strongly influences
the dynamics of the fluid particles. This solvent model is then coupled to
a molecular dynamics simulation algorithm. We obtain excellent agreement
between our simulation results for a flexible polymer and the predictions of
Zimm theory. The study of the translational diffusion coefficient of rod-like
polymers confirms the predicted chain-length dependence. In addition, we
study the influence of shear on the structural properties of rod-like polymers. For
shear rates exceeding the rotational relaxation time, the rod-like molecule aligns
with the shear flow, leading to an orientational symmetry breaking transverse
to the flow direction. The comparison of the obtained shear rate dependencies
with theoretical predictions exhibits significant deviations. The properties of
the orientational tensor and the rotational velocity are discussed in detail as a
function of shear rate.

1. Introduction

The equilibrium and nonequilibrium dynamical behaviour of complex fluids like dilute and
semi-dilute polymer solutions, colloidal suspensions and microemulsions, is strongly affected
by the hydrodynamic interaction. Its adequate inclusion in a theoretical description of such
systems has been a long-standing problem. From a simulation point of view, molecular
dynamics simulations with explicit consideration of solute and solvent take into account

---

[1] Author to whom any correspondence should be addressed.

hydrodynamic interactions. However, most of the simulation time is used to evaluate the solvent dynamics in great detail, which is not necessary to achieve the proper hydrodynamic behaviour on the colloidal or polymer length scale.

The large length- and time-scale gap between the solvent molecules and the solute calls for a coarse-grained and simplified description of the solvent dynamics. This has led to the development of novel mesoscopic simulation techniques. Prominent examples are lattice models such as lattice-gas automata [1] and lattice-Boltzmann methods [2–6], and particle based off-lattice methods such as dissipative particle dynamics [7–10] and multi-particle-collision dynamics (MPCD) [11–13]. The latter method is also called stochastic rotation dynamics (SRD) [14] or the Malevanets–Kapral method [15].

A mesoscale simulation technique has to account for the correlated motion of solvent particles which leads to long-range hydrodynamic interactions. In this dynamic regime, viscous momentum transport dominates over diffusive transport. A measure for this ratio is the Schmidt number Sc, which is defined as $Sc = \nu/D$, where ν is the kinematic viscosity and D the diffusion coefficient. Fluids are characterized by large Schmidt numbers $Sc \approx 10^2$–10^3 compared to $Sc \approx 1$ of gases. Considering colloidal systems, this corresponds to the Stokes regime, in which the hydrodynamic interaction is typically approximated by the Oseen tensor (or a similar tensor) in analytical theories [16, 17].

In this paper, we briefly show that the MPCD algorithm is able to account for hydrodynamic interactions for a proper choice of model parameters like the mean free path of a solvent particle. As an example, we present results for the dynamics of flexible polymer chains in dilute solution [17]. In particular, we discuss the dependence of the Rouse mode relaxation times on the mode number and show that they are in excellent agreement with the predictions of the Zimm theory [16, 18].

Flow fields strongly affect the conformational properties of flexible polymers. The orientation and deformation of such molecules have been studied by flow birefringence [19, 20], light scattering [21, 22] and neutron scattering [23], and have also been investigated by nonequilibrium molecular dynamics simulations [24–29].

Apart from flexible polymers there is a large class of polymers which assume a rod-like structure [16]. The physical properties of the latter polymers differ from those of the flexible ones. One aspect is the large anisotropy of such molecules. Thus, they are much more easily oriented in an external field, e.g., in shear flow. This enables experimental studies using electric or magnetic birefringence as a practical tool to study the rotational motion of these polymers.

Theoretical treatment of rod-like polymers is much easier than of flexible polymers, since rod-like polymers can have only two kinds of motion, i.e. translation and rotation. Various results are presented in [16]. However, the dynamics of rod-like polymers in dilute solution is also affected by hydrodynamic interactions, which are not always possible to take properly into account in analytical theories. Although the influence of hydrodynamic interactions on the rotational and translational diffusion is weak—there is only a logarithmic correction with respect to chain length—to our knowledge there is no systematic study on the effect of the hydrodynamic interaction on, e.g., the orientational tensor and the rotational velocity of rods in dilute solution under the influence of shear flow. However, various studies indicate a complex rotational dynamics of rod-like liquid crystals [30–32].

In the following, we will present a systematic study of the dependence of the orientational tensor on the shear rate of a rod-like polymer in shear flow. Our results partially confirm the theoretical predictions in [16]. We find, however, also significant deviations in particular in the flow regime where the rod is oriented by the flow.

The paper is organized as follows. In section 2, the simulation method is described and the properties of the solvent are discussed in section 3. The equilibrium dynamical properties

of flexible and rod-like polymers in dilute solution are briefly discussed in sections 4 and 5. In section 6, the nonequilibrium dynamics of rod-like molecules in shear flow is studied. Finally, section 7 summarizes our findings.

2. Simulation method

The solvent is described as a system of N, typically 10^5–10^6, point-like particles of mass m moving in continuous space. Depending on the problem under investigation, three-dimensional periodic boundary conditions are applied, or surfaces are explicitly introduced, combined with two-dimensional periodic boundary conditions. The MPCD algorithm consists of two steps. In the streaming step, the particles move ballistically. Hence, their positions ($r_i, i = 1, \ldots, N$) change according to

$$r_i(t + h) = r_i(t) + h v_i(t), \tag{1}$$

where v_i denotes the velocities of the particle i and h is the time between collisions.

In the collision step, the particles are sorted into cubic cells of lattice constant a. For a cubic simulation box of side length L, the average number of particles per cell is $\rho = Na^3/L^3$. Then, the velocity of each particle is rotated relative to the centre of mass velocity v_{cm} of all the particles within that cell according to

$$v_i(t + h) = v_{cm}(t) + \mathcal{R}(\alpha)(v_i(t) - v_{cm}(t)). \tag{2}$$

$\mathcal{R}(\alpha)$ is the rotation matrix for the rotation by a fixed angle α. The orientation of the rotation axis is chosen randomly for every collision cell and time step [33, 34]. To insure Galilean invariance of the simulation scheme, a random shift is applied before every collision step [14, 35]. The MPCD algorithm conserves mass, energy and momentum for every collision cell, and hence also globally. There is a H-theorem for the algorithm for large [11] and small mean free paths [35], and it yields in the first case the correct hydrodynamic equations with an ideal gas equation of state [11, 36].

A polymer chain is introduced into the system by adding N_m point particles of mass M. Depending on the considered system, different bond potentials were used.

In order to compare our simulation results with the predictions of the Zimm model, we used the potential

$$U_R = \frac{3k_B T}{2l^2} \sum_{i=1}^{N_m-1} (r_{i+1} - r_i)^2 \tag{3}$$

corresponding to the Rouse model [16]. Here, T is the temperature, k_B the Boltzmann constant and l the root mean square bond length.

In our study of rod-like polymers, we applied the bond potential

$$U_S = \frac{\kappa_S}{2} \sum_{i=1}^{N_m-1} (|r_{i+1} - r_i| - l)^2, \tag{4}$$

where κ_S is the spring constant which we chose rather large to avoid stretching of the bonds [37]. To obtain rod-like conformations, the bending potential

$$U_B = \kappa_B \sum_{i=1}^{N_m-2} (r_{i+1} - r_i)(r_{i+2} - r_{i+1}) \tag{5}$$

is employed [38]. The force constant κ_B is determined in such a way that the mean square end-to-end distance is $0.98(N_m - 1)^2 l^2$.

Newton's equations of motion for a chain molecule are integrated by the velocity Verlet algorithm with the time step h_p. To account for the monomer–solvent interaction, the monomers are included in the collision step equation (2), i.e. in collision cells containing monomers, the centre of mass is calculated by taking the monomers into account and also the velocities of the monomers are rotated [39]. The new velocities are used to continue the integration of the monomer trajectories.

Finally, we introduced dimensionless variables by scaling length and time according to $\hat{r} = r/a$ and $\hat{t} = t\sqrt{k_B T m/a^2}$, which corresponds to the choice $k_B T = 1$, $m = 1$ and $a = 1$. The mean free path of a solvent particle $h\sqrt{k_B T/m}$ is then given by $\lambda = \hat{h}$.

3. Solvent dynamics

The solvent mediates the hydrodynamic interaction among solute particles. Hence, the adequate simulation of the solvent dynamics is essential to achieve the proper behaviour for particle-based mesoscale simulation techniques. In particular, it is desirable to have control over the viscosity and the Schmidt number.

The total viscosity η of the MPCD algorithm consists of a kinetic contribution η_{kin} and a collisional contribution η_{col} for which the approximate analytical expressions

$$\eta_{kin} = \frac{k_B T h \rho}{a^3}\left(\frac{5\rho}{(4 - 2\cos\alpha - 2\cos 2\alpha)(\rho - 1)} - \frac{1}{2}\right), \tag{6}$$

$$\eta_{col} = \frac{m(1 - \cos\alpha)}{18ha}(\rho - 1) \tag{7}$$

have been derived in three dimensions [15, 33–35]. To determine the viscosity ($\eta = \eta_{kin} + \eta_{col}$) by simulations, we confined the fluid between two walls and applied an external field to induce a Poiseuille flow [13, 33, 34, 40]. Periodic boundary conditions are present in the transverse directions. By using bounce-back boundary conditions at the surfaces, we obtain parabolic velocity profiles. Exploiting the solution of the Navier–Stokes equation for the Poiseuille flow, the maximum velocity gives us the fluid viscosity.

Figure 1 displays the kinematic viscosity $\nu = \eta/\rho$ as a function of the rotation angle (left) and the collision time (right). The figure exhibits very good agreement between the analytical expression and the simulation results. As is obvious from the figure, for large α and small collision times the collisional viscosity dominates over the kinetic one. Thus, a large viscosity is obtained for small h values and large densities ($\eta = \rho\nu$) [17].

The presence of the hydrodynamic interaction is reflected in the velocity autocorrelation function. Assuming molecular chaos and averaging over the random orientations of the rotational axis, the following expression can be derived from equation (2) for the velocity autocorrelation function [15, 35] for a particle i

$$\langle \boldsymbol{v}_i(nh)\boldsymbol{v}_i(0)\rangle = (1 - \gamma)^n \langle v_i^2(0)\rangle, \tag{8}$$

where $\gamma = 2(\rho - 1)(1 - \cos\alpha)/(3\rho)$ and n is the number of collision steps. Figure 2 depicts the velocity autocorrelation function for a system of $N = 135\,000$ particles with $\hat{\rho} = 5$ particles per cell on average for the rotation angle $\alpha = 130°$. It reveals a qualitative and quantitative different behaviour of the fluid for the mean free paths $\lambda = 1$ and 0.1, respectively. For $\lambda = 1$, the correlation function decays exponentially over several decades and exhibits for large times a long time tail. This is in agreement with the above theoretical expression, as shown by the thin dashed line. At short times, the particles exhibit thermal Brownian dynamics, whereas the hydrodynamic interaction plays a dominant role for larger times. The function (8) yields a faster decay for the smaller collision times $\lambda = 0.1$. However, for the small mean free path,
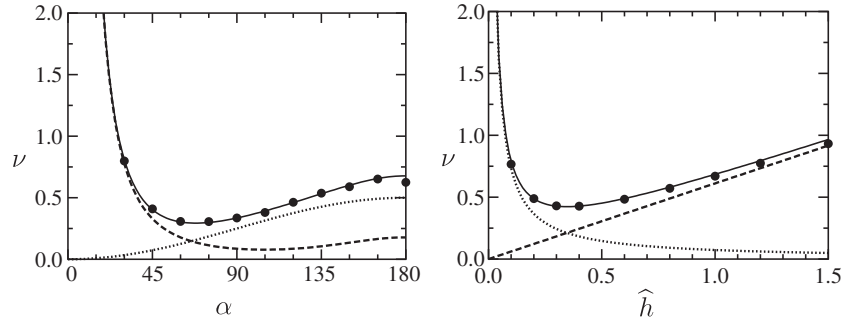
Figure 1. Kinematic viscosity for a simple fluid of the MPCD algorithm. The symbols indicate simulation results and the curves are calculated according to analytical expressions. The dotted curves represent the collisional contribution (7) and the dashed curves the kinetic contribution (6) to the total viscosity. The system size is $L = 20a$. For the dependence of ν on the rotation angle (left), $\hat{h} = 0.2$ and $\hat{\rho} = 10$ is used, whereas for the dependence on the collision time (right), $\alpha = 130°$ and $\hat{\rho} = 5$ is used.
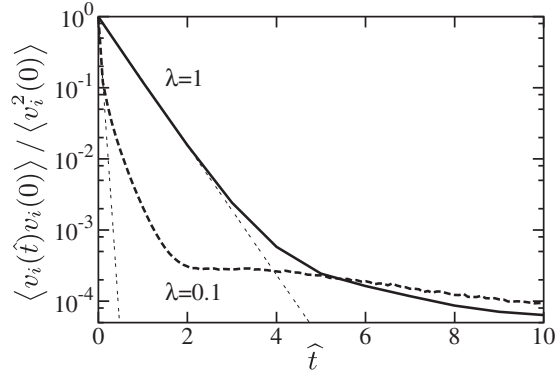

Figure 2. Velocity autocorrelation function as a function of time for the mean free paths $\lambda = 1$ and 0.1. The thin dashed lines correspond to the exponential decay according to equation (8). The number of fluid particles is $\hat{\rho} = 5$ and the rotation angle is $\alpha = 130°$.

strong correlations build up among the particles that slow down the relaxation and the correlation function no longer decays exponentially. We attribute these correlations to the hydrodynamic interaction in the system. The analytical term is now in quantitative agreement with the simulation results for the first step only. The reason is that the molecular chaos assumption applies for the initial distribution of velocities [17].

The self-diffusion coefficient follows from the velocity autocorrelation function via the Green–Kubo relation or can be extracted from the mean square displacement. Starting from the equation of motion for the fluid, the following expression for the mean square displacement is obtained by applying the molecular chaos assumption [41]

$$\left\langle (r_i(nh) - r_i(0))^2 \right\rangle = h^2 \left\langle v_i^2(0) \right\rangle \left(n \left(\frac{2}{\gamma} - 1 \right) - 2 \frac{1-\gamma}{\gamma^2} \left(1 - (1-\gamma)^n \right) \right). \tag{9}$$

In the limit $n \gg 1$, the mean square displacement is a linear function of n with the diffusion coefficient

$$D = h \frac{k_B T}{m} \left(\frac{1}{\gamma} - \frac{1}{2} \right). \tag{10}$$

Our simulation results are very well described by equation (9) for $\lambda > 0.6$. The velocity autocorrelation function shown in figure 2 demonstrates that the correlation has decayed several orders of magnitude before the long-time tail appears. Hence, the latter does not
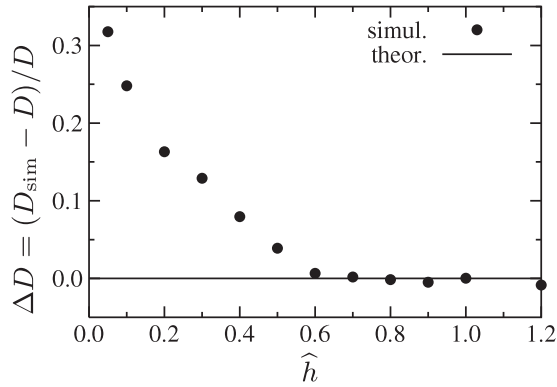
Figure 3. Relative difference of the numerically determined diffusion constant and the theoretically predicted value according to equation (10) as a function of collision time. The same parameters as in figure 2 are used.

contribute significantly to the diffusion coefficient, which is thus given by equation (10). For smaller collision times h however, the hydrodynamic interaction yields an increased diffusion coefficient compared to the theoretical value (10). Figure 3 displays the deviation between the diffusion constant obtained from the simulation and the theoretical expression (10). Obviously, the relative difference increases with decreasing h, which reflects the increasing influence of the hydrodynamic interaction for small collision time steps.

As already pointed out in the introduction, the ratio between hydrodynamic transport and diffusion is expressed by the Schmidt number $Sc = \nu/D$. Using the expressions of equations (6), (7), and (10), respectively, we find $Sc \approx 1$ for the mean free path $\lambda = 1$ and $Sc \approx 10$ for $\lambda = 0.1$. The comparison of the contributions of the collisional and kinetic viscosity to the total kinematic viscosity shows that at large mean free paths the kinetic contribution dominates, whereas at small λ the collisional contribution is dominating. Thus, we conclude that a collisional viscosity significantly larger than the kinematic one is important for the observation of hydrodynamic effects. Within the MPCD algorithm, we are able to adjust the Schmidt number by choosing an appropriate collision time step. A large ν_{col} follows for small h and since $D \sim h$ and $\nu_{col} \sim 1/h$, the Schmidt number exhibits the dependence $Sc \sim 1/h^2$ [17].

4. Dynamics of flexible polymers in dilute solution

The dynamics of polymer chains in dilute solution is strongly affected by the hydrodynamic interaction. Experiments on such systems confirmed the predictions of Zimm theory on flexible polymers almost quantitatively [16]. Thus, the verification of the dependencies of the centre-of-mass diffusion coefficient and of the relaxation times on the chain length as well as the predicted dependence of the relaxation times on the mode number is a stringent test for any simulation algorithm incorporating hydrodynamic interactions.

To demonstrate the usefulness of the proposed simulation scheme we studied the dynamics of flexible polymer chains of lengths $N_m = 5, 10, 20, 40, 80$ and 160 employing the bond potential (3). The average number of fluid particles per cell was set to $\hat{\rho} = 10$, the rotation angle to $\alpha = 150°$, and the mean free path to $\lambda = 0.1$. Thus, the collisional viscosity is larger than the kinetic one. The system size was changed linearly with the radius of gyration $R_g = l\sqrt{(N_m - 1)(N_m + 1)/6N_m}$ to avoid artifacts due to the finite system sizes [42]. Explicitly, for $N = 20$ we chose a cubic periodic simulation box of length $18a$. In addition, we set the monomer mass to $M = 10m$. The time step for the integration is $\hat{h}_p = 10^{-2}$.

To characterize the internal dynamics, we performed a mode analysis in terms of the eigenfunctions of the discrete Rouse model [16, 43]. The mode amplitudes are
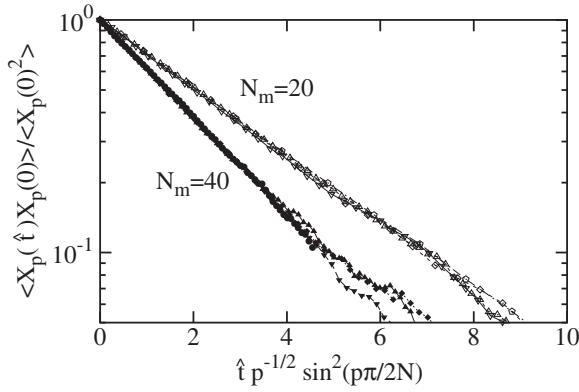
Figure 4. Correlation functions of the Rouse mode amplitudes for various modes (1–4). The chain lengths are $N_m = 20$ and 40. The mean free path is $\lambda = 0.1$ and the density is $\hat{\rho} = 10$.

calculated according to

$$\chi_p = \sqrt{\frac{2}{N_m}} \sum_{i=1}^{N_m} \boldsymbol{r}_i \cos\left[\frac{p\pi}{N_m}\left(i - \frac{1}{2}\right)\right]. \tag{11}$$

Due to hydrodynamic interactions, Rouse modes are no longer eigenfunctions of the chain molecule. However, within the approximations of the Zimm theory [16, 18], they are reasonable approximations and the autocorrelation functions of the mode amplitudes decay exponentially, i.e. $\langle \chi_p(t)\chi_p(0) \rangle = \langle \chi_{pl}^2 \rangle \exp\left(-t/\tau_p\right)$. For the Rouse model, the relaxation times τ_p depend on chain length and mode number according to $\tau_p \sim 1/\sin^2(p\pi/N_m)$, whereas for the Zimm model the dependence $\tau_p \sim (p/N_m)^{1/2}/\sin^2(p\pi/N_m)$ is obtained. Thus, the calculation of the relaxation times is a crucial test for the presence of hydrodynamic interactions.

In figure 4 the autocorrelation functions for the mode amplitudes are shown for the mean free path $\lambda = 0.1$. Within the accuracy of our simulations, the correlation functions decay exponentially and exhibit the scaling behaviour according to the Zimm model. Hence, for the mean free path $\lambda = 0.1$ hydrodynamic interactions are taken into account correctly. We obtain pure Rouse behaviour [16, 43] without solvent by simply rotating the velocities of the individual monomers, i.e. without subtraction of the centre-of-mass velocity of each cell in equation (2). In [42], a correction term to the standard Zimm result has been derived. Such a correction is not needed to achieve agreement of our data with the predictions of the Zimm model, nor do our data support the existence of such a term. Hence, we conclude that other approximations in the derivation of the Zimm results compensate for these corrections [17].

Calculating the centre of mass diffusion constant for various chain lengths, we find the dependence $D \sim R_g^{-1}$ [17], where R_g is the root mean square radius of gyration, in agreement with the prediction of the Zimm theory as well as other mesoscale simulations [39, 44, 45].

A comparison of the centre-of-mass diffusion constant extrapolated to an infinite system with the value of the Zimm theory shows that the value extracted from simulations is approximately 20% smaller. Moreover, the relaxation time of the $p = 1$ mode is only approximately 30% ($N_m = 40$) larger than the Zimm value.

Sufficiently long Zimm relaxation times compared to the decay of the velocity autocorrelation function are required to observe the dynamics in the Stokes regime. Hence, in the simulation the relaxation times (also for higher modes) should be longer than the time required to reach the regime where the mean square displacement of the centre of mass of a polymer becomes linear. To reach this regime we can change the kinematic viscosity of the fluid, or, since $\eta = \rho\nu$, change the fluid density. By choosing $\hat{\rho} = 10$, this prerequisite for the Zimm dynamics is fulfilled in our simulations.
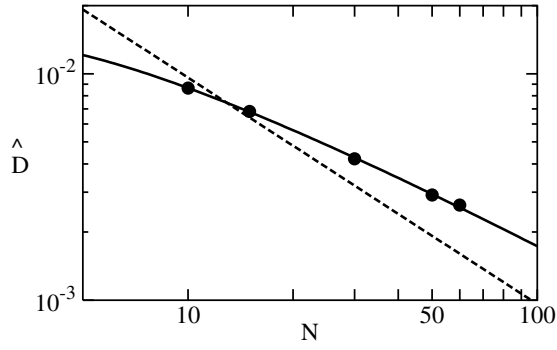
Figure 5. Centre of mass translational diffusion constant of rod-like molecules for various chain lengths. The dots represent simulation results and the solid curve is calculated according to the theoretical equation (12). The dashed line corresponds to $\hat{D}_G \sim 1/(N_m - 1)$.

5. Dynamics of rod-like polymers in dilute solution

The hydrodynamic interaction also affects the equilibrium dynamics of rod-like polymers. Its influence on the centre of mass translational diffusion coefficient, however, is much less pronounced. An analytical calculation yields the relation [46]

$$D_G = \frac{k_B T}{3\pi\eta L_m} \left[\frac{\ln(L_m/b)}{L} + 0.316 \right] \tag{12}$$

(up to the order b/L), where b is the diameter and $L_m = (N_m - 1)l$ is the length of the rod [16].

To verify this relation, we performed simulations of single rod-like molecules with up to $N_m = 60$ beads and the parameters $l = a/2$, $\hat{h} = 0.1$, $\alpha = 150°$, $M = 5m$, $\hat{\rho} = 5$ and $\hat{h}_p = 2 \times 10^{-3}$. To avoid artifacts in the determination of the chain length dependence due to finite system size effects, the size of the cubic simulation box is increased linearly with the length of the rod, where we chose $L = 9a$ for $N_m = 10$ [42].

Figure 5 shows our simulation results together with the theoretical curve (12), where we determined $D_0 = k_B T/(3\pi\eta)$ and b by a least squares fit. This procedure yields $\hat{D}_0 = 0.02$, where the hat indicates that the diffusion constant is expressed in the units introduce at the end of section 2, and $b = 0.84a$. D_0 is approximately 20% smaller than the value of the solvent. The deviation is most likely a consequence of the finite system size, because we did not extrapolate our results to an infinite system. The thickness b is reasonable in size, since it is close to the bond length and the size of a collision cell. The dashed line corresponds to a dependence $D_G \sim 1/L_m$. The simulation results obviously do not follow a simple $1/L_m$ dependence, which would be expected for a rod without hydrodynamic interaction, but are very well described by the theoretically predicted dependence (12). Hence, the hydrodynamic interaction is once more well captured by the MPCD algorithm.

6. Rod-like polymer in shear flow

To study the stationary state properties of rod-like polymers under shear flow, we used a three-dimensional periodic system and applied Lees–Edwards boundary conditions along the y-axis, where the flow velocity field is $v = (\dot{\gamma} y, 0, 0)^T$ with the shear rate $\dot{\gamma}$ [47]. A random orientation of the unit vector u, pointing along the end-to-end distance of the rod, was chosen for the initial conformation and Maxwellian distributed velocities were assigned to the mass points. The temperature was kept constant by scaling the velocities of the fluid particles along the vorticity direction. The other parameters are the same as for the equilibrium simulations except for the mass of a monomer which we set to $M = 10m$ and the density of fluid particles which is $\hat{\rho} = 10$. To study the effect of shear flow, we varied the shear rate over more than three
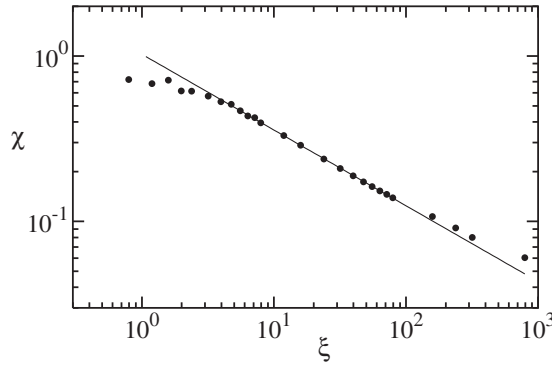
Figure 6. Orientation angle χ as a function of the reduced shear rate $\xi = \dot{\gamma}/D_r$. For shear rates $\xi > 5$, χ obeys the power law $\chi \sim \xi^{-0.46}$.

orders of magnitude. The averages presented in the following are obtained by time averages over trajectories of individual runs and over 10^3 independent initial conformations.

The systems become anisotropic by the applied shear field. The shear induced deviations from the equilibrium values are measured by tensorial quantities. Since the director u uniquely characterizes the orientation of the rod-like molecule, the orientational tensor

$$S_{\alpha\beta} = \langle u_\alpha u_\beta \rangle - \tfrac{1}{3}\delta_{\alpha\beta} \tag{13}$$

($\alpha, \beta \in \{x, y, z\}$) can be used to measure the anisotropy of the system [16]. For a rod-like object, this expression is closely related to the gyration tensor [28]

$$G_{\alpha\beta} = \sum_{i=1}^{N_m} \Delta r_\alpha^i \Delta r_\beta^i = G\left(S_{\alpha\beta} + \tfrac{1}{3}\delta_{\alpha\beta}\right), \tag{14}$$

where $\Delta r_i = r_i - r_{cm}$ and r_{cm} is the centre of mass position of the polymer. For a rod-like molecule, the trace of the gyration tensor $G = \sum_\alpha G_{\alpha\alpha}$ is a constant.

The alignment of the molecule with respect to the flow direction can be quantified by the flow-alignment angle χ in terms of the orientational tensor via

$$\cot(2\chi) = \frac{S_{xx} - S_{yy}}{2S_{xy}}. \tag{15}$$

Figure 6 presents the orientation angle as a function of shear rate, where $\xi = \dot{\gamma}/D_r$ is the dimensionless shear rate (sometimes called rotational Peclet number) and D_r is the rotational diffusion coefficient, which is related to the rotational correlation time τ_r via $\tau_r = 1/2D_r$ [16]. The analysis of simulations at zero shear rate yields a rotation diffusion coefficient $\hat{D}_r \approx 1.3 \times 10^{-3}$ (for the finite system). For small shear rates ($\xi < 2$), χ is close to $\pi/4$, which corresponds to the equilibrium value without flow. With increasing shear rate, the alignment angle decreases according to the power law $\chi \sim \xi^{-0.46}$. Simulations of flexible polymers in shear flow [28] yield almost exactly the same exponent.

In [16], the following expressions are derived for the orientational tensor using a decoupling approximation

$$S_{xy}\left(1 + \tfrac{1}{3}\xi S_{xy}\right) = \tfrac{1}{18}\xi + \tfrac{1}{6}\xi S_{yy}, \tag{16}$$

$$S_{xx} = \frac{2\xi S_{xy}}{9(1 + \xi S_{xy}/3)}, \tag{17}$$

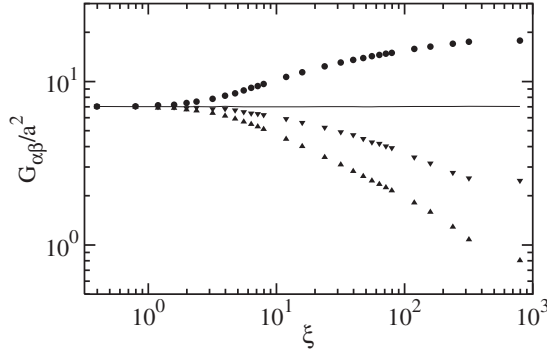$$S_{yy} = S_{zz} = -\tfrac{1}{2}S_{xx}. \tag{18}$$

Figure 7. Diagonal components of the gyration tensor (14): G_{xx} (bullets), G_{yy} (upper triangles) and G_{zz} (lower triangles). The solid line is 1/3 of the sum of the individual components. It demonstrates that the length of the polymer is constant for the various shear rates.
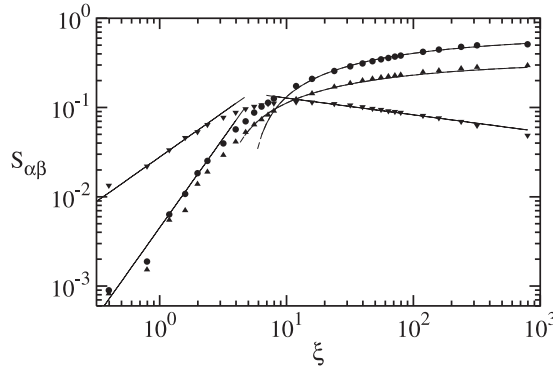

Figure 8. Components S_{xx} (bullets), $-S_{yy}$ (upper triangles) and S_{xy} (lower triangles) of the orientational tensor as a function of the reduced shear rate. The solid lines are calculated according to $\sim \xi$ and $\sim \xi^2$, respectively, at $\xi < 3$. For $\xi > 10$, the simulation results are well described by $S_{xy} \sim \xi^{-1/4}$ and $S_{\alpha\alpha} = S_{\alpha\alpha}^{\infty} - \kappa_{\alpha\alpha} \xi^{-1/3}$ with $S_{xx}^{\infty} = 2/3$ and $S_{yy}^{\infty} = -1/3$.

In the appropriate limits, these expressions reduce to

$$S_{xy} = \begin{cases} \dfrac{1}{18}\xi, & \xi \ll 1 \\[2mm] \dfrac{1}{(2\xi)^{1/3}}, & \xi \gg 1, \end{cases} \tag{19}$$

$$S_{xx} = \begin{cases} \dfrac{1}{81}\xi^2, & \xi \ll 1 \\[2mm] \dfrac{2}{3} - 2\left(\dfrac{2}{\xi^2}\right)^{1/3}, & \xi \gg 1. \end{cases} \tag{20}$$

Figure 7 displays the diagonal elements of the gyration tensor. For shear rates $\xi < 1$, the systems are isotropic and hence the diagonal components of $G_{\alpha\beta}$ are equal. With increasing shear rate, the rod-like molecule aligns along the shear flow and G_{xx} increases. The other components decrease accordingly. The two components perpendicular to the flow direction, however, exhibit different shear rate dependencies, in particular, G_{yy} decays much faster than G_{zz}. As a consequence, the relations of equation (18) do not apply for $\xi > 1$. This is also obvious from figure 8.

Comparing the numerical determined components of the orientational tensor with the theoretical predictions, we find several deviations. As shown in figure 8 the relation $S_{yy} = S_{zz} = -S_{xx}/2$ is not valid. We rather find that $S_{yy} \approx -2S_{xx}/3$ for small shear rates. With increasing shear rate, the two curves split.

The comparison of the dependence of S_{xx}, S_{yy} and S_{xy}, respectively, on the reduced shear rate for $\xi < 3$, yields good agreement with respect to the predicted powers. The numerical factors, however, are significantly different. For shear rates $\xi > 10$, the predictions (19)
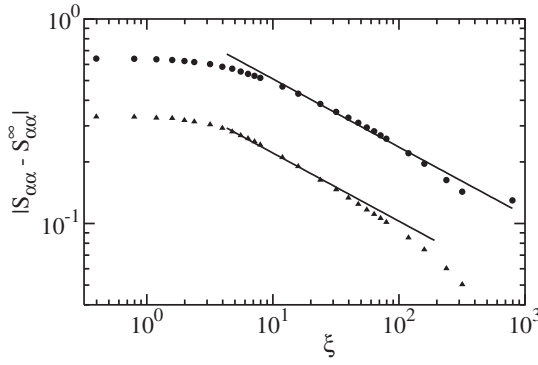
Figure 9. Dependence of the orientational tensor on the shear rate. The straight lines are calculated according to $|S_{\alpha\alpha} - S_{\alpha\alpha}^{\infty}| \sim \xi^{-1/3}$, with $S_{xx}^{\infty} = 2/3$ (bullets) and $S_{yy}^{\infty} = -1/3$ (triangles).

and (20) do not apply. A least square fit for S_{xy} yields good agreement with the dependence $S_{xy} \sim \xi^{-1/4}$. To extract the limiting behaviour of S_{xx} and S_{yy} at $\xi > 10$, we performed a least square fit of these curves with the functions $S_{\alpha\alpha} = S_{\alpha\alpha}^{\infty} - \kappa_{\alpha\alpha}\xi^{-1/3}$ ($\alpha \in \{x, y\}$). As shown in figure 8, the simulation data can very well be described by such a dependence. In particular, we obtain $S_{xx}^{\infty} = 2/3$ and $S_{yy}^{\infty} = -0.35$. The first factor agrees with the theoretically predicted value (20), which is consistent with the fact that G_{xx} approaches G in the limit $\xi \to \infty$. $S_{yy}^{\infty} = -0.35$ is close to the predicted value $-1/3$, the difference could be a consequence of statistical uncertainties. Thus, we use $S_{yy}^{\infty} = -1/3$ for further discussion. Figure 9 shows that $|S_{\alpha\alpha} - S_{\alpha\alpha}^{\infty}|$ is well described by the dependence $|S_{\alpha\alpha} - S_{\alpha\alpha}^{\infty}| \sim \xi^{-1/3}$. The component S_{zz} of the orientational tensor depends on the other two diagonal elements, since the director u is normalized.

We finally discuss the rotational velocity ($\omega = (\omega_x, \omega_y, \omega_z)^{\mathrm{T}}$) of the rod-like molecule and its dependence on shear rate. The rotational velocity of a rigid body can be obtained from the relation $L = \Theta\omega$, where the angular momentum $L = (L_x, L_y, L_z)^{\mathrm{T}}$ and the tensor of inertia Θ, with respect to the centre of mass, are given by

$$L = \sum_{i=1}^{N_m} M \Delta r_i \times \Delta \dot{r}_i, \tag{21}$$

$$\Theta_{\alpha\beta} = \sum_{i=1}^{N_m} M \left(\Delta r_i^2 \delta_{\alpha\beta} - \Delta r_\alpha^i \Delta r_\beta^i \right). \tag{22}$$

The rotational velocity with respect to the z-axis is the given by

$$\omega_z = \sum_{\alpha \in \{x,y,z\}} \Theta_{\alpha z}^{-1} L_\alpha. \tag{23}$$

A relation between the angular momentum, the gyration tensor, and the shear rate can be established in the following way. When fluctuations are neglected, the velocity in the angular momentum (21) can be replaced by the local velocity of the flow field ($\Delta \dot{r}_i \approx v(r_i)$). With $v(r_i) = (\dot{\gamma}\Delta y_i, 0, 0)^{\mathrm{T}}$, the z-component of L becomes then

$$\langle L_z^G \rangle = -\dot{\gamma} M \langle G_{yy} \rangle \tag{24}$$

in terms of the y-component of the gyration tensor. Here we use the symbol L_z^G to express its approximate character and to distinguish it from the expression in terms of the inertia tensor. On the other hand, if we neglect the off-diagonal elements of the inertia tensor (21) and replace Θ_{zz} by its average, we find

$$\langle L_z \rangle \approx \langle \Theta_{zz} \rangle \bar{\omega}_z = M(\langle G_{xx} \rangle + \langle G_{yy} \rangle)\bar{\omega}_z. \tag{25}$$
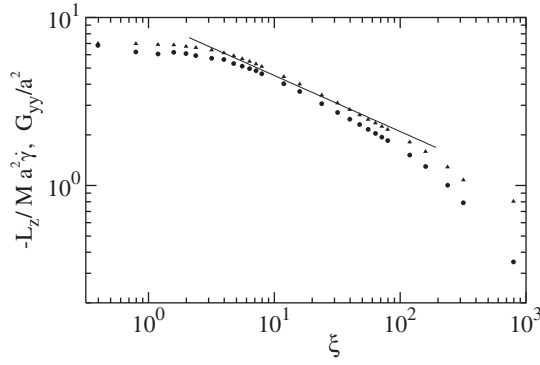
Figure 10. Scaled angular momentum $-L_z/\dot{\gamma}M$ (bullets) and G_{yy} of the gyration tensor (triangles) as a function of shear rate. The line represents the power law $\xi^{-1/3}$.
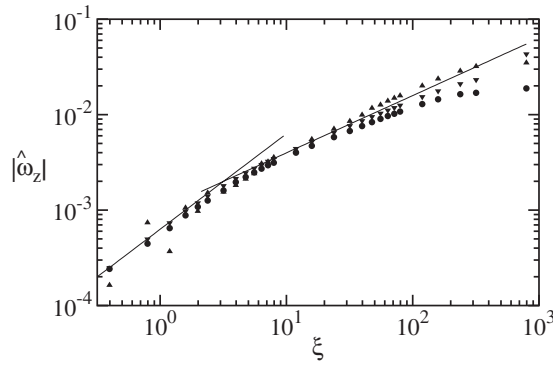

Figure 11. Rotational velocities according to the expressions (23) (ω_z, upper triangles), (26) ($\bar{\omega}_z$, bullets) and (27) (ω_G, lower triangles) as functions of the shear rate. The solid line at small shear rates is calculated according to $\omega_z = -\dot{\gamma}/2$. For large shear rates, the solid line is given by $\omega_z \sim -\xi^{0.6}$.

The symbol $\bar{\omega}_z$ again indicates that approximations are involved in its calculation. Combining equations (24) and (25), the rotational frequencies

$$\bar{\omega}_z = \frac{\langle L_z \rangle}{M \left(\langle G_{xx} \rangle + \langle G_{yy} \rangle \right)}, \tag{26}$$

$$\omega_G = -\dot{\gamma} \frac{\langle G_{yy} \rangle}{\langle G_{xx} \rangle + \langle G_{yy} \rangle} \tag{27}$$

are obtained. The same expressions have been derived in [29]. Since the system is isotropic for $\dot{\gamma} \to 0$, one finds $\omega_G = -\dot{\gamma}/2$ in this limit.

Figure 10 displays the z-component of the angular momentum (21) in the scaled form $(-L_z/\dot{\gamma}M)$ together with the y-component of the gyration tensor. If the two expressions agree, equation (24) is valid. Aside from a shift of about 10%, the two expressions indeed agree very well. The deviations at high shear rates are due to insufficient statistical accuracy. G_{yy} decays to zero with increasing shear rate, hence a large ensemble is required to obtain precise results at high shear rates. In particular, the two quantities decrease with increasing shear rate in a qualitative similar manner. The solid line represents the power law $\xi^{-1/3}$. This dependence describes the decay approximately. A somewhat large exponent would describe the data more closely. However, the factor $-1/3$ is consistent with the exponent extracted from the orientational tensor.

The angular velocities are presented in figure 11. We included the values calculated via equations (23) (ω_z), (26) ($\bar{\omega}_z$) and (27) (ω_G). The magnitude of the angular frequencies increases with increasing shear rate in agreement with expectation. Like for the curves in figure 10, the angular frequencies $\bar{\omega}_z$ and ω_G deviate approximately by 10%. Otherwise the

curves display the same dependence on shear rate. For $\xi < 2$, the angular velocity decreases linearly with the shear rate and ω_z obeys the equation $\omega_z = -\dot{\gamma}/2$ as shown by the solid line. For large shear rates, a second regime appears, where the magnitude of the angular velocity increases more slowly. The solid line plotted in figure 11 for this regime represents the power law $\xi^{0.6}$. This value accounts for the simulation data quite well. The angular velocity ω_z increases somewhat faster than $\bar{\omega}_z$ with the shear rate for $\xi > 10$. This is due to different fluctuations encountered in the calculation of averages. For $\bar{\omega}_z$ and ω_G, mean values for the angular momentum and the gyration tensor are used, whereas for $\omega_z' \langle \boldsymbol{\omega} \rangle = \langle \boldsymbol{\Theta}^{-1} \boldsymbol{L} \rangle$ is used, i.e. the product is averaged. Despite this difference, the various angular velocities display qualitatively the same dependence on shear rate.

7. Summary and conclusions

In this paper we discussed the transport properties of the MPCD algorithm and applied it to studies of the equilibrium and nonequilibrium dynamics of flexible and rod-like molecules. We outlined that for the appropriate choice of parameters, i.e. for collision time steps $\hat{h} \lesssim 0.1$ and rotation angles $\alpha > 90°$, collisional transport dominates over kinetic transport and hydrodynamic interactions are taken into account properly. The scaling behaviour of the Rouse mode amplitudes of flexible polymers in dilute solutions is a stringent test for the incorporation of hydrodynamic interactions in a simulation algorithm. Our simulation results agree excellently with the prediction of the Zimm model. Considering the translational diffusion constant of a rod-like molecule in dilute solution, we obtain agreement with the theoretically predicted logarithmic dependence on the chain length. These two examples confirm our conclusions on the suitability of the MPCD method to simulate complex systems in a solution based on the results of simple fluids.

In addition, we studied orientational and dynamical properties of rod-like molecules in shear flow. For shear rates exceeding the rotational relaxation time, the molecule aligns along the flow direction. The flow-alignment angle decreases with increasing shear according to a power law. Interestingly, flexible chains in shear flow exhibit the same power law [28] (within the accuracy of the simulations). The shear induced orientation of the rod leads to a breakdown of the orientational symmetry in the gradient and vorticity direction. As is reflected in the gyration tensor, the component along the vorticity direction decays much slower with shear than the component along the gradient direction. This is in contrast to theoretical calculations presented in [16]. The decoupling approximation exploited in [16] seems to be a too crude approximation, in particular at large shear rates. Comparing the theoretically predicted dependencies of the components of the orientational tensor with the simulation results, we find the predicted exponents ε of the relation ξ^ε for weak flow rates. The front factors are, however, rather different. At shear rates above the rotational relaxation time, our simulations suggest significantly smaller exponents than those predicted by the theory [16].

Considering the angular momentum in the vorticity direction, we confirmed the tight connection between the angular momentum and the gyration tensor. The ratio ($-L_z/\dot{\gamma}M$ ($-L_z/\dot{\gamma}M$)) decays within 10% deviations similarly to G_{yy}. The magnitude of the rotational frequency itself increases linearly at small shear rates. In the regime where the molecule is aligned with respect to the flow direction, the rotational velocity increases much slower. All of the considered expressions for the angular velocity exhibit the same shear rate dependence within the accuracy of the simulations.

To overcome the discrepancies between the simulation results and the theoretical calculations [16], refined analytical calculations are necessary. Such calculations are currently under way. In addition, it would be useful to perform simulations of longer rods. Since the

director of the rod uniquely determines its orientation, however, we do not expect a significant chain length dependence of the predicted dependencies.

Acknowledgments

References

[1] Frisch U, Hasslacher B and Pomeau Y 1986 *Phys. Rev. Lett.* **56** 1505
[2] McNamara G R and Zanetti G 1988 *Phys. Rev. Lett.* **61** 2332
[3] Benzi R, Succi S and Vergassola M 1992 *Phys. Rep.* **222** 145
[4] Ladd A J C 1994 *J. Fluid Mech.* **271** 311
[5] Chen S and Doolen G D 1998 *Annu. Rev. Fluid Mech.* **30** 329
[6] Ahlrichs P and Dünweg B 1998 *Int. J. Mod. Phys.* C **9** 1429
[7] Hoogerbrugge P J and Koelman J M V A 1992 *Europhys. Lett.* **19** 155
[8] Español P and Warren P 1995 *Europhys. Lett.* **30** 191
[9] Groot R D and Warren P B 1997 *J. Chem. Phys.* **107** 4423
[10] Ripoll M, Ernst M H and Español P 2001 *J. Chem. Phys.* **115** 7271
[11] Malevanets A and Kapral R 1999 *J. Chem. Phys.* **110** 8605
[12] Malevanets A and Kapral R 2000 *J. Chem. Phys.* **112** 7260
[13] Lamura A, Gompper G, Ihle T and Kroll D M 2001 *Europhys. Lett.* **56** 319
[14] Ihle T and Kroll D M 2001 *Phys. Rev.* E **63** 020201(R)
[15] Kikuchi N, Pooley C M, Ryder J F and Yeomans J M 2003 *J. Chem. Phys.* **119** 6388
[16] Doi M and Edwards S F 1986 *The Theory of Polymer Dynamics* (Oxford: Clarendon)
[17] Ripoll M, Mussawisade K, Winkler R G and Gompper G 2004 *Europhys. Lett.* at press
[18] Zimm B H 1956 *J. Chem. Phys.* **24** 269
[19] Janeschitz-Kriegl H J 1969 *Adv. Polym. Sci.* **6** 170
[20] Peterlin A 1976 *Annu. Rev. Fluid Mech.* **8** 35
[21] Cottrell F R, Merrill E W and Smith K A 1969 *J. Polym. Sci.* A 2 **7** 1415
[22] Zisenis M and Springer J 1995 *Polymer* **36** 3459
[23] Lindner P and Oberthür R C 1989 *Physica* B **156/157** 410
[24] Pierleoni C and Ryckaert J-P 1991 *Phys. Rev. Lett.* **61** 2992
[25] Pierleoni C and Ryckaert J-P 1992 *J. Chem. Phys.* **96** 8539
[26] Pierleoni C and Ryckaert J-P 1995 *Macromolecules* **28** 5097
[27] Hess S 1987 *J. Non-Newton. Fluid Mech.* **23** 305
[28] Aust C, Kröger M and Hess S 1999 *Macromolecules* **32** 5660
[29] Aust C, Kröger M and Hess S 2002 *Macromolecules* **35** 8621
[30] Szeri A J 1995 *J. Rheol.* **39** 873
[31] Rienäcker G, Kröger M and Hess S 2002 *Physica* A **315** 537
[32] Chillingworth D R J, Alonso E V and Wheeler A A 2001 *J. Phys. A: Math. Gen.* **34** 1393
[33] Allahyarov E and Gompper G 2002 *Phys. Rev.* E **66** 036702
[34] Allahyarov E and Gompper G 2003 *Phys. Rev.* E **67** 059901
[35] Ihle T and Kroll D M 2003 *Phys. Rev.* E **67** 066705
[36] Tüzel E, Strauss M, Ihle T and Kroll D M 2003 *Phys. Rev.* E **68** 036701
[37] Winkler R G, Gold M and Reineker P 1998 *Phys. Rev. Lett.* **80** 3731
[38] Winkler R G, Reineker P and Harnau L 1994 *J. Chem. Phys.* **101** 8119
[39] Malevanets A and Yeomans J M 2000 *Europhys. Lett.* **52** 231
[40] Lamura A and Gompper G 2002 *Eur. Phys. J.* **9** 477
[41] Ihle T and Kroll D M 2003 *Phys. Rev.* E **67** 066706
[42] Ahlrichs P and Dünweg B 1999 *J. Chem. Phys.* **111** 8225
[43] Rouse P E 1953 *J. Chem. Phys.* **21** 1272
[44] Schlijper A G, Hoogerbrugge P J and Manke C W 1995 *J. Rheol.* **39** 567
[45] Spenley N A 2000 *Europhys. Lett.* **49** 534
[46] de la Torre J G and Bloomfield V A 1981 *Q. Rev. Biophys.* **14** 81
[47] Allen M P and Tildesley D J 1987 *Computer Simulation of Liquids* (Oxford: Clarendon)